DE GRUYTER

Pure Appl. Chem. 2023; 95(6): 671–682

Special topic paper

Silvia Carlotto*, Luca Babetto, Marzio Rancan, Gregorio Bottaro, Maurizio Casarin and Lidia Armelao*

How to get deeper insights into the optical properties of lanthanide systems: a computational protocol from ligand to complexes

Abstract: Theoretical calculations are proving as an essential tool to understand luminescence processes even for systems including lanthanide (Ln^{3+}) ions. As such, the aim of this study is that of presenting a general and comprehensive theoretical protocol based on DFT calculations to rationalize and possibly drive the design of new luminescent Ln^{3+} complexes through the ab initio determination of the electronic properties of a ligand and two Eu^{3+} complexes. Different theoretical methodologies have been combined to look into the excited state energies, the luminescence quantum yield, and the energy transfer processes. The protocol has been validated for a β-diketone ligand and two Eu^{3+} complexes, which contain, in addition to the main ligand, ethanol or triphenyl-phosphine oxide. Moreover, by starting from the geometry optimization up to the estimation of the ligands' singlet and triplet lowest energy states, theoretical results quantitatively agree with luminescence experimental parameters, providing at the same time insights into the different energy transfer processes. The different quantum yields of the two complexes have been correctly reproduced.

Keywords: Computational chemistry; inorganic chemistry; lanthanides; luminescence; Mary L. Good.

1 Introduction

In the last decades, technological development contributed to a huge of lanthanide (Ln) chemistry [1–4]. Indeed, they find applications in several fields ranging from organic light-emitting devices [5–7], magnetic devices [8], chemosensors [9], luminescent thermometers [10], to tumour target bioimaging [11–13] or in general to the drug delivery monitoring [14–16] to name just a few but very relevant functionalities. More specifically, ternary

*Corresponding authors: Silvia Carlotto, Department of Chemical Sciences (DiSC), University of Padova, via F. Marzolo 1, 35131 Padova, Italy; Institute of Condensed Matter Chemistry and Technologies for Energy (ICMATE), National Research Council (CNR), c/o Department of Chemical Sciences (DiSC), University of Padova, via F. Marzolo 1, 35131 Padova, Italy; and National Interuniversity Consortium of Materials Science and Technology (INSTM), Florence, Italy, e-mail: silvia.carlotto@unipd.it ; and **Lidia Armelao**, Department of Chemical Sciences (DiSC), University of Padova, via F. Marzolo 1, 35131 Padova, Italy; National Interuniversity Consortium of Materials Science and Technology (INSTM), Florence, Italy; and Department of Chemical Sciences and Materials Technologies (DSCTM), National Research Council (CNR), Piazzale A. Moro 7, 00185 Rome, Italy, e-mail: lidia.armelao@unipd.it
Luca Babetto and Maurizio Casarin, Department of Chemical Sciences (DiSC), University of Padova, via F. Marzolo 1, 35131 Padova, Italy
Marzio Rancan and Gregorio Bottaro, Institute of Condensed Matter Chemistry and Technologies for Energy (ICMATE), National Research Council (CNR), c/o Department of Chemical Sciences (DiSC), University of Padova, via F. Marzolo 1, 35131 Padova, Italy; and National Interuniversity Consortium of Materials Science and Technology (INSTM), Florence, Italy

β-diketonate europium complexes have large relevance [17] as red emitters in electroluminescence devices [18], as temperature sensors [19], as laser devices [20] or as luminescence probes in biological systems [21].

Now, despite the gigantic amount of papers devoted every year to lanthanide complexes, only a small fraction of them involves computational tools and computer-driven protocols [22], which might support experimental studies focused on the design of more efficient luminescence systems [23–25] or more sensitive thermometers devices [19, 26–28]. Among the electronic properties theoretically achievable, the ligands' excited triplet state plays a pivotal role in several photophysical and reactive phenomena due to the so-called "antenna effect" for the sensitization of lanthanide emission [3]. Indeed, the energy gap between the ligand excited triplet state (T_1) and the Ln^{3+} emitter level ($^5D_0$), $\Delta E(T_1 - {}^5D_0)$, is one of the key factors to evaluate the luminescence properties. In particular, an efficient ligand $\rightarrow$ metal energy transfer (ET) implies $2500\ cm^{-1} < \Delta E(T_1 - {}^5D_0) < 4000\ cm^{-1}$ [29], while a higher sensitivity in luminescence thermometers [19, 26–28, 30–32] needs *ca.* $20\ cm^{-1} < \Delta E(T_1 - {}^5D_0) < 1500\ cm^{-1}$ [33, 34]. Theoretical ligand energy levels and transition moments may be then combined to estimate the ET and back-ET rates between the ligands and the Ln^{3+} ion, allowing the evaluation of both the quantum yield (PLQY) and the weight between the radiative and non-radiative paths for the luminescence processes [17].

In this study, a general and comprehensive DFT-based protocol is proposed to rationalize, and possibly to drive, the design of luminescent Ln^{3+} complexes through an ab initio determination of the electronic properties of a ligand and two selected Eu^{3+} complexes'. The protocol will be herein validated for two Eu^{3+} tris(β-diketonate) complexes, whose coordination chemistry and photo-physics properties have been recently published [19]. The β-diketone ligand (**L**) we considered features two thienyl groups, while the two Eu^{3+} complexes, in addition to **L**, have two auxiliary ligands: ethanol in $EuL_3(EtOH)_2$ (hereafter, **EuL₃E₂**) or triphenylphosphine oxide (TPPO) in $EuL_3(TPPO)_2$ (hereafter, **EuL₃T₂**) (see Fig. 1).

The final goal is beyond that of finding the origin of the different **EuL₃E₂**/**EuL₃T₂** behaviour and instead to propose a computational protocol able to quantitatively reproduce the observed trend by calculating luminescence quantum yields, radiative (A_{rad}) and non-radiative (A_{nrad}) decay rates, ET and back-ET contributions starting from the **L** lowest singlet (S_1) and triplet (T_1) excited states to Eu^{3+} selected excited states ($^5D_4$, $^5D_1$ and $^5D_0$). Different methodologies and software packages have been combined to get the best agreement with experimental evidence at every single step of the protocol, from geometry optimization to the T_1 energy up to the luminescence quantum yield. The forthcoming discussion is organized into three sections: (i) the first one is devoted to the modelling of the structural properties of **L** and of the Eu^{3+} complexes and then compared with single crystal X-ray diffraction (SCXRD) data; (ii) the second is focused on the rationalization of the absorption spectra of **L**, **EuL₃E₂** and **EuL₃T₂** and (iii) the third one is dedicated to the modelling the **EuL₃E₂** and **EuL₃T₂** luminescence behaviour by exploiting the excited states properties and intermolecular energy transfer (IET) processes.
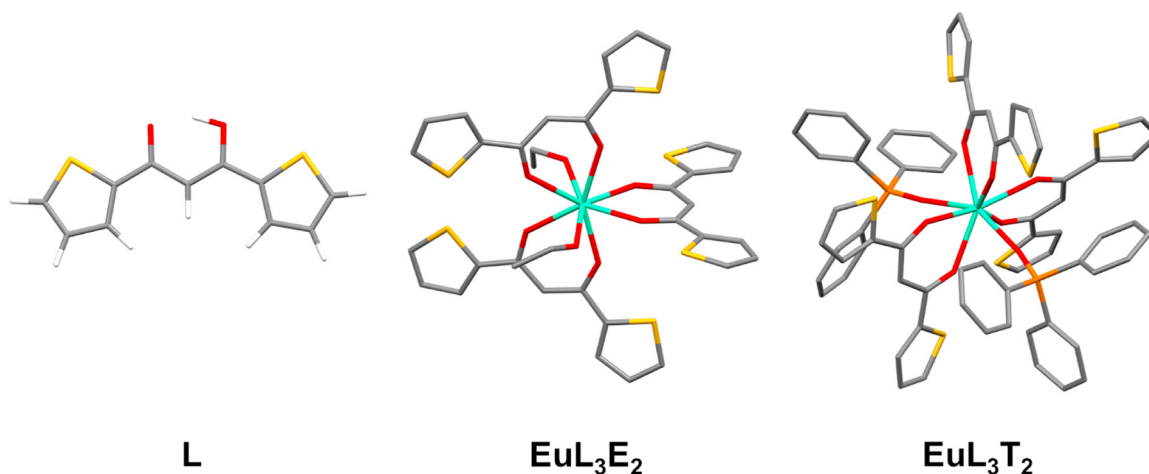

L   **EuL₃E₂**   **EuL₃T₂**

Fig. 1: L, **EuL₃E₂** and **EuL₃T₂** complexes obtained from the optimized structures (PBE level). Yellow, white, grey, red, green and orange sticks are S, H, C, O, Eu and P atoms, respectively. In the complexes, H atoms are omitted for clarity.

2 Results and discussion

2.1 Ground state geometries for L, EuL₃E₂ and EuL₃T₂

Positional disorder in X-ray crystal structure (CCDC 1539534) suggests that **L** occurs as two rotamers (Fig. S1; hereafter, A and B) whose percentages amount to $85 \pm 0.5\%$ (A) and $15 \pm 0.5\%$ (B) [35]. In A, both thiophene rings "point" in the same directions, with two S atoms on the same side of the diketone oxygen atoms, while in B the S atoms point at opposite sides. Geometrical parameters of both A and B have been optimized by adopting either the PBE or the B3LYP functionals and, independently of the adopted exchange-correlation (XC) functional, A resulted more stable than B (0.39 kcal/mol and 0.50 kcal/mol in PBE and B3LYP calculations, respectively). All computational details for calculations are reported in Supplementary Information. If a Boltzmann population is assumed for the two rotamers and the energy differences are taken into account, the theoretical distribution at room temperature (RT, 298.15 K) can be obtained by:

$$P_i = \frac{e^{\frac{\varepsilon_i}{k_B T}}}{Q} \tag{1}$$

$$Q = \sum_i e^{\frac{\varepsilon_i}{k_B T}} \tag{2}$$

where P_i is the population of the i-th rotamer, ε_i is the energy of the i-th rotamer, k_B is the Boltzmann constant and T is the temperature. B3LYP and PBE distributions (69.9 %/30.1 % and 65.9 %/34.1 %, respectively) are very similar and in satisfactory agreement with crystallographic data (optimised structures perfectly match the crystallographic geometries (Fig. S2)), with tiny better accordance for B3YLP. The small difference between theoretical and experimental distributions may be due to crystal packing effects, which cannot be modelled in single molecule calculations. Before going on, it deserves to be emphasized that a third rotamer C with both thiophene rings pointing in the same direction but with the S atoms on the opposite side of the diketone oxygen atoms (Fig. S1) could be present. Even though C has not been experimentally revealed, it has been included in our analyses. Indeed, its absence in the solid state does not necessarily rule out its possible presence in the solution. As such, C is less stable than A by 1.83 kcal/mol and the B3LYP Boltzmann populations of A, B and C correspond to 68 %, 29 % and 3 %, respectively. To verify whether different forms may undergo interconversion, a linear transit calculation has been carried out. At RT, only a negligible fraction (corresponding to 10^{-9} of the molecules) would possess sufficiently high energy to overcome the 8 kcal/mol barrier; thus, possible interconversion phenomena have been neglected (details on this matter are reported in the Supplementary Information (Fig. S3)). Even though solvent effects have been considered for A, it has to be underlined that the corresponding B3LYP and PBE optimised structures are perfectly superimposable to the gas-phase ones, thus confirming that the geometry optimisation of small organic molecules experimentally found either in the crystal phase or dissolved in an apolar solvent can be confidently carried out by exploiting gas phase calculations [36, 37].

X-ray data for **EuL₃E₂** (CCDC 1539532) and **EuL₃T₂** (CCDC 1539535) are reported in ref [19, 35] and corresponding geometries have been used as a starting point for the geometry optimisation calculations. To simplify the comparison between theoretical and experimental structures, the following key quantities have been monitored throughout the numerical experiments: (i) internuclear distances between Eu^{3+} and the coordinated O atoms of **L**; (ii) the angle formed by the O atoms of **L** and Eu; (iii) the angle formed by Eu and the central C atoms of two distinct **L** (see Fig. S4). In fact (i) and (ii) provide information about the Eu^{3+} coordination environment, while (iii) supply details about the **L** relative orientation. The comparison of the **EuL₃E₂** and **EuL₃T₂** optimized geometrical parameters with the experimental outcomes (see Tables S1 and S2, respectively) reveals the very good agreement between experiment and theory (Fig. S5), with the Eu-O distances slightly overestimated by ~2 % on average (see Table S3). Again, tiny deviations may be tentatively attributed to crystal packing phenomena. Before moving to the analysis of spectroscopic data, let us emphasise that B3LYP and PBE geometrical parameters are very similar (Fig. S6), with the former performing slightly better than the latter but at a significantly higher

computational cost: the **EuL₃E₂** B3LYP geometry optimisation took 17 times more CPU time than the PBE one with the same starting geometry. As the differences between B3LYP and PBE optimized geometries are almost negligible, **EuL₃T₂** calculations have been carried out by exploiting only the PBE functional (the PBE optimised geometry of **EuL₃T₂** is compared with its X-ray structure in Fig. S7). As a whole, DFT calculations provide a reliable prediction of the ground state geometry of the Eu^{3+} complexes and the optimised structures are in very good agreement with X-ray data.

2.2 L, EuL₃E₂ and EuL₃T₂ absorption spectra

The **L** absorption spectrum has a single broad band in the near UV region (around 375 nm) and two evident shoulders at 395 and 360 nm (Fig. 2, solid line).

   TD-DFT numerical experiments have been carried out by exploiting diverse XC functionals (SAOP, LB94, PBE0 and B3LYP) and by using the B3LYP optimized ground state geometry. Regardless of the adopted XC functional, the near UV region includes only one intense transition (Fig. 2a and Table S4) involving the highest occupied molecular orbital (HOMO) and lowest unoccupied molecular orbitals (LUMO), both of them delocalized over the whole molecule (Fig. 2b). PBE0 and B3LYP XC functionals overestimate the HOMO–LUMO ΔE, a well-known hybrid functional drawback [38, 39], while the agreement between experiment and theory for SAOP and LB94 functional, specifically designed to estimate excitation energies, is somehow better. More specifically, the SAOP HOMO–LUMO ΔE (385 nm) lies very close to the absorption spectrum's highest intensity peak (375 nm), while the LB94 one (400 nm) is at the edge of the spectrum, close to the lower energy shoulder (395 nm). As a whole, the absolute position of vertical transitions indicates that the SAOP XC functional provides the best numerical agreement between experiment and theory. Literature results pertaining to β-diketones ligands formed by a thienyl group and different polycyclic aromatic hydrocarbons (naphthyl, phenanthryl and pyrenyl) are consistent with the results herein reported [26]. Despite such a semi-quantitative agreement, we cannot be silent about the failure of the tested XC functionals in reproducing the presence of the different shoulders characterizing the absorption spectrum of **L**. Indeed, an accurate simulation of the excited state energies is a key factor to reproduce luminescence properties and hopes to drive the design and the synthesis of new materials.

   Besides the electronic transitions, it is well known that the absorption spectrum shape is determined by different factors such as the presence of (i) diverse **L** geometrical isomers (such as rotamers); (ii) different **L**
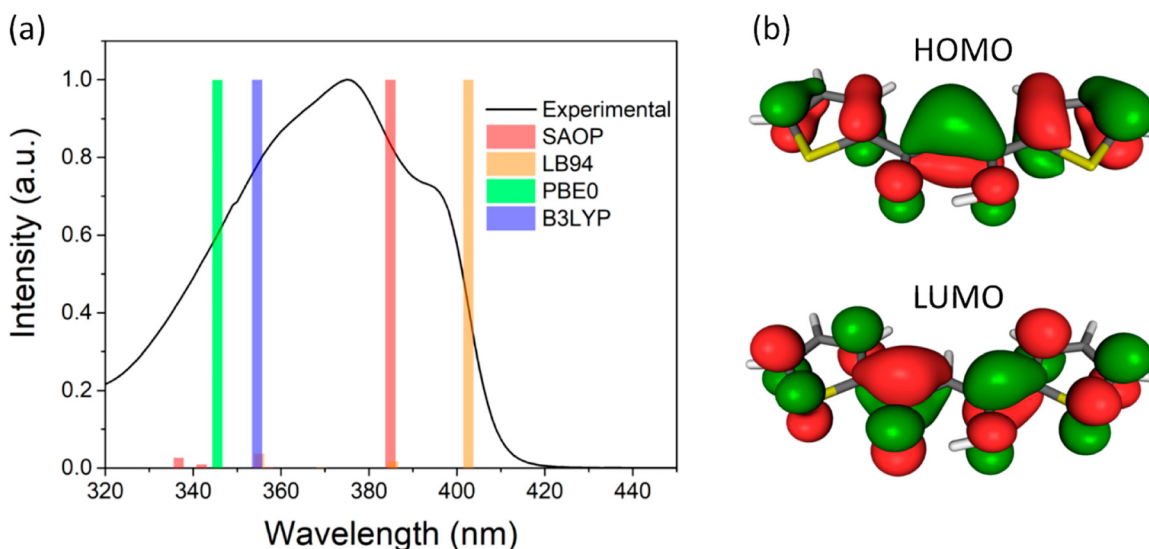

Fig. 2: Normalized experimental absorption spectrum of **L** (solid black line) recorded in solution (toluene) superimposed to the different theoretical vertical excitation energies on the rotamer A estimated by adopting the B3LYP optimised ground state geometry but diverse XC functionals (SAOP, LB94, PBE0, B3LYP) (a). 3D plots of the MOs mainly contribute to the electronic transition (b).

structural isomers (keto-enol tautomerism in β-diketone ligands) and (iii) vibronic progression based on the Franck–Condon principle. The shoulders' origin in the **L** absorption spectrum has been then rationalized by individually considering, via DFT methods, all these factors. The absorption spectra of rotamers A, B and C have been modelled with both SAOP and LB94 functionals and, for all the rotamers, only one high-intensity TD-DFT transition (~385 nm) is present in the UV–Vis region (see Fig. S8). The shoulders characterizing the **L** absorption spectrum cannot be then attributed to the presence of different **L** rotamers in solution and different factors need to be explored.

Even though the **L** NMR data are consistent with the coexistence of both enol and ketone isomers, the former species is strongly prevalent [35], perfectly in agreement with the optimized B3LYP geometry of **L** in its enolic form, more stable than that corresponding to the keto isomer of 6.84 kcal/mol, probably as a consequence of the higher electronic delocalisation taking place in the enol species (see in Fig. S9 the strongly localized nature of the HOMO in the ketone isomer). It has been already mentioned that a single electronic HOMO–LUMO transition at 385 nm is expected for the enol isomer on the basis of TD-DFT/SAOP calculations (see Fig. 2), while, in agreement with the literature data of Suwa et al. [40] which assigned the far UV region (~260 nm) of the absorption spectrum of **L** in acetonitrile to the ketone isomer, the corresponding theoretical spectrum is characterized by several excitations around 270 nm. Thus, the ketonic form of **L** cannot be invoked to explain the shape of its spectrum in the region of interest (320–420 nm), which would seem to be then determined by the vibronic progression. As such, it is useful to remind that TD-DFT only considers purely electronic transitions, i.e., no vibrational components are included. The modelling of a vibrationally resolved spectrum needs the evaluation of Franck-Condon factors. Specifically, the theoretical vibrational progression has to be offset by taking into account the energy of the corresponding electronic transition, and the vibrationally resolved spectrum is obtained. Now, as the hybrid B3LYP and PBE XC functionals are not well suited to estimate excitation energies, only the LB94 and SAOP electronic transitions will be considered in the forthcoming discussion.

SAOP and LB94 vibrationally resolved absorption spectra of the rotamer A are superimposable, as they are both obtained by means of a Franck-Condon analysis carried out by adopting either the PBE or the B3LYP XC functional (see Fig. 3), the only difference being the opposite wavelength shift they need to match the recorded spectrum. Nevertheless, it has to be noted that the PBE Franck-Condon analysis is negligibly affected by the adopted number of vibrational quanta, while the B3LYP vibrational progression dramatically changes if transitions may also start from the first excited vibrational state (see Fig. 3). In even more detail, the agreement between experiment and theory is quantitative if ground state vibrationally excited levels are taken into account:
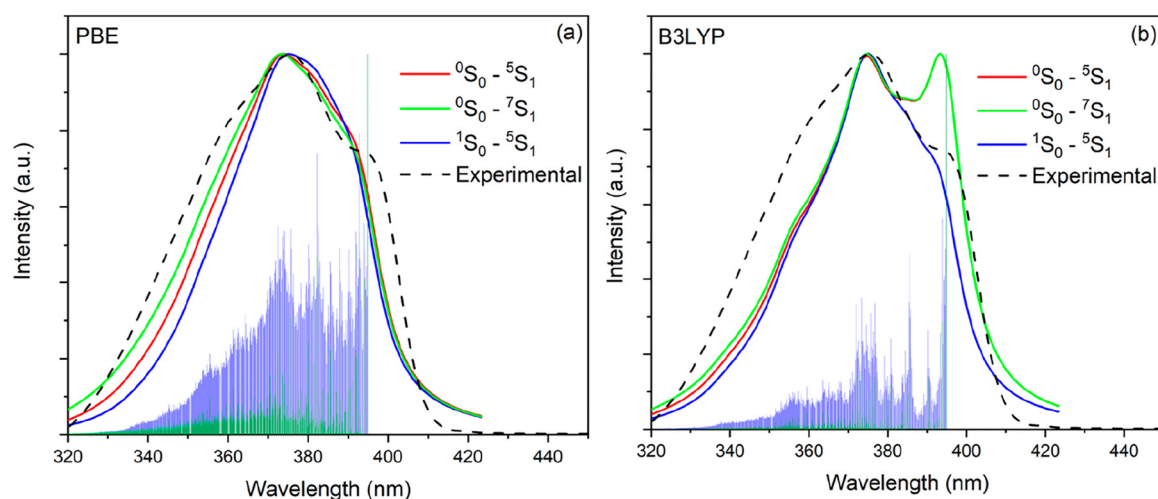

Fig. 3: Normalized vibrationally resolved absorption spectra for the rotamer A of **L**. The calculated spectra have been redshifted by 10 nm from the HOMO → LUMO transition calculated at the TD-DFT/SAOP level. Geometries and frequencies were calculated with PBE (a) and B3LYP (b). Convoluted profiles have been obtained by using a Lorentzian broadening of 0.05 eV.

the shoulders on the lower and higher wavelength side are estimated at 19 nm and 18 nm from the main peak, respectively. These two values in the experimental spectrum are 20 nm and 19 nm, respectively. As a whole, the adoption of the B3LYP functional and the inclusion of the vibronic progression not only allow a satisfactory mimicking of the absorption spectrum but also of the emission luminescence one (Fig. S11). Further details are reported in the Supplementary Information.

The role played by **L** in determining the **EuL$_3$E$_2$** and **EuL$_3$T$_2$** electronic properties and corresponding absorption spectra may be better appreciated by considering how spectral features vary upon moving from the free **L** to the Eu^{3+} complexes. The close similarity of the spectra (see Fig. 4a) suggests that the absorption properties are mainly determined by **L**, the main difference being a weak shoulder at ~420 nm in the **EuL$_3$T$_2$** spectrum (see Fig. 4a).

Aimed to look into the origin of this feature, the **EuL$_3$E$_2$** and **EuL$_3$T$_2$** spectra have been then modelled. To minimize the corresponding computational cost, only electronic transitions have been considered while vibrational contributions to the spectra have been neglected. Once again, TD-DFT numerical experiments have been carried out by exploiting both LB94 and SAOP XC functionals (see Fig. 4b and c). Interestingly, at variance to **L**, whose 320–500 nm spectral region includes only the HOMO → LUMO transition, the spectra of both **EuL$_3$E$_2$** and **EuL$_3$T$_2$**, independently of the adopted XC functionals, are characterized by several high- and low-intensity excitations whose initial and final states are mainly generated by L-based HOMOs and LUMOs, respectively. As such, it is worthwhile to remind that the three ligands in **EuL$_3$E$_2$** and **EuL$_3$T$_2$** are not equivalent (Fig. S12). In addition, the likeness of the most intense electronic transition in **EuL$_3$E$_2$** and **EuL$_3$T$_2$** further supports the assumption that the complex spectra are scarcely affected by the Eu^{3+} presence. As far as low-intensity transitions are concerned, they both involve ligand-to-ligand charge transfer (CT) and, especially for **EuL$_3$T$_2$** ligand-to-metal (LMCT) transition. The LMCT minor contribution to the absorption spectra confirms that the **L** electronic properties are negligibly affected by the presence of the metal centre [26].

TD-DFT calculations may be also useful to look into the Eu^{3+} local environment if the attention is focused on *4f–4f* transitions. Even though such analysis might be useful to thoroughly characterise the complexes, its detailed description is beyond the scope of the protocol and it is reported in the Supplementary Information.

2.3 EuL$_3$E$_2$ and EuL$_3$T$_2$ luminescence: excited states properties and intermolecular energy transfer (IET) process

The two complexes have different lifetimes and quantum yields: 60.7 μs and 0.4 % for **EuL$_3$E$_2$**, 170.8 μs and 5.0 %, for **EuL$_3$T$_2$** respectively [19]. Quite confidently, the **EuL$_3$T$_2$** longer lifetime may be attributed to the C$_2$H$_5$OH absence [19]. Indeed, ethanol increases the non-radiative decay rate (A$_{nrad}$) and deactivates the ^{5}D$_0$ excited state of

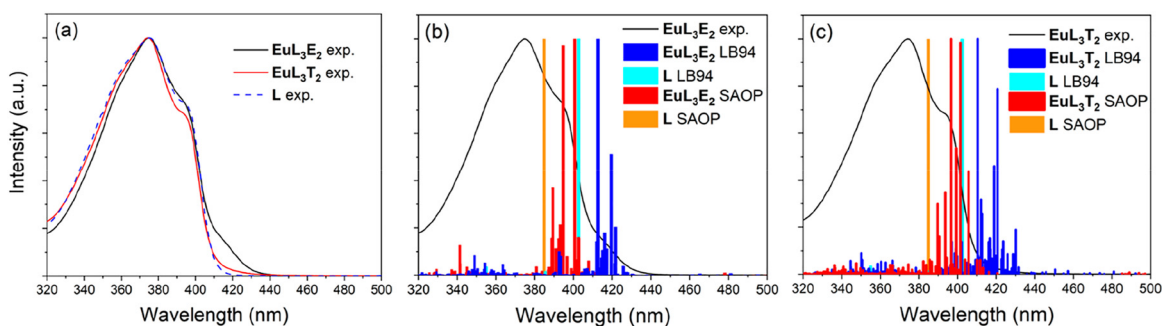**Fig. 4:** Normalized experimental (a) and simulated (b, c) UV–Vis spectra for **EuL$_3$E$_2$** (b) and **EuL$_3$T$_2$** (c). Simulated spectra are obtained at the TD-DFT/SAOP and TD-DFT/LB94 levels by using the optimised PBE geometries. Electronic transitions of the free L have been also included for comparison..

Eu^{3+} [19, 41, 42]. Rather than looking for the origin of the different spectroscopic properties of **EuL_3E_2** and **EuL_3T_2**, our goal is the quantitative reproduction of the experimental quantum yield PLQY and to obtain quantum efficiency, A_{rad}, A_{nrad}, the energy transfer rate (W_{ET}) and the back-energy transfer rate (W_{BT}) values by combining experimental data (lifetime and emission spectrum) and TD-DFT calculations (energies of the **L** lowest singlet (S_1) and triplet (T_1) excited states). In addition, the literature Eu^{3+} selected ($^5D_4$, $^5D_1$ and $^5D_0$) excited states are used, whose choice has been determined by the evidence that the $^5D_0$ state may be populated by three paths: (i) the energy transfer (ET) from S_1 to $^5D_4$ and then, for non-radiative decay, to $^5D_0$; (ii) the ET from T_1 to $^5D_1$ and then, for non-radiative decay, to $^5D_0$ or (iii) a direct ET from T_1 to $^5D_0$. The weights of the different paths are related to W_{ET} and W_{BT}.

To rationalise and then quantify the different roles played by **L** and Eu^{3+}, the energies of the **L** S_1 and T_1 excited states need to be known accurately. As such, the role of the triplet may be experimentally determined by substituting the Eu^{3+} ion with the Gd^{3+} one both in **EuL_3E_2** and **EuL_3T_2**: **GdL_3E_2** and **GdL_3T_2** emissions from S_1 (fluorescence) and T_1 (phosphorescence) excited states lie at *ca.* 23,800 cm^{-1} and *ca.* 18,900 cm^{-1}, respectively [19]. As far as the theoretical modelling is concerned, a highly accurate T_1 energy is crucial because the ΔE between T_1 and the Eu^{3+} excited states $\Delta E(T_1 - {}^5D_0)$ is tightly bound to the quantum efficiency. Indeed, the T_1 state must be higher in energy than the Eu^{3+} excited state ($^5D_0$) to prevent the back-ET from the Eu^{3+} emitting state to T_1, which would favour the luminescence quenching. As recently shown in a study with **L** = β-diketonate [26], the T_1 energy may be estimated through two distinct approaches: (i) the vertical transition (VT) approach [43] either as the lowest energy $S_0 \rightarrow T_1$ TD-DFT vertical transition in the GS optimized geometry or as the lowest energy $T_1 \rightarrow S_0$ TD-DFT vertical transition in the T_1 optimized geometry; (ii) the adiabatic transition – AT approach [44], as the $\Delta E(T_1 - S_0)$ with both states in their optimised geometries (see Fig. S13). AT and VT T_1 energies have been estimated for **L**, **EuL_3E_2** and **EuL_3T_2** as well as for **LaL_3E_2** and **LaL_3T_2** (see Table S6). According to the literature [26], the best-suited approach is the AT one and corresponding **L** T_1 energies will be herein used to investigate the **EuL_3E_2** and **EuL_3T_2** ET processes. A detailed analysis of VT and AT values is reported in the Supplementary Information.

To model the L – Eu^{3+} ET, both the ET and the decay rates were evaluated by employing the LUMPAC code [22], where, in addition to TD-DFT results, the experimental spectrum for the Judd-Ofelt intensity parameters (omega) and the lifetime are necessary to gain quantum yield PLQY, quantum efficiency, A_{rad}, A_{nrad}, W_{ET} and W_{BT} values. As far as Eu^{3+} is concerned, the ET has been modelled by considering only the three states $^5D_4$, $^5D_1$ and $^5D_0$ (see above), whose energy values are fixed in the code; as far as **L** is concerned, the S_1 and T_1 energies must be computed. Despite LUMPAC would allow their estimate, the evaluation of T_1 energies at the INDO/S-CI levels is significantly and systematically underestimated when compared with the experiment (see Table S7). Diverse geometries (PBE optimized geometry, X-ray data and Sparkle/RM1 optimized geometry) have been tested to evaluate the LUMPAC T_1 energy; its values resulted in systematically underestimated by ~3–4000 cm^{-1} and then a negligible energy transfer (Table S8). On the contrary, TD-DFT calculations combined with the AT approach provide T_1 values, which better agree with the experiment. On this basis, the **L** S_1 and T_1 energies have been estimated at the DFT/SAOP level and used as input in LUMPAC to evaluate all the parameters useful to quantitatively model the **EuL_3E_2** and **EuL_3T_2** ET mechanism. In particular, A_{rad}, A_{nrad}, quantum efficiency, and PLQY for both complexes are shown in Table 1.

Table 1: LUMPAC values for the radiative (A_{rad}) and nonradiative (A_{nrad}) decay rates, quantum efficiency, and quantum yield PLQY are reported obtained from experimental lifetimes of 60.7 μm (**EuL_3E_2**) and 170.8 μm (**EuL_3T_2**). In parentheses, PLQY experimental values. Ligand state energies (S_1 and T_1) are calculated at the TD-DFT SAOP and AT levels of theory, respectively.

	EuL_3E_2	EuL_3T_2
A_{rad} (s^{-1})	661	1143
A_{nrad} (s^{-1})	15814	4712
Quantum efficiency (%)	4.01	19.52
PLQY (%)	0.67 (*0.4*)	3.48 (*5.0*)

The emission quantum yield PLQY value is a relevant parameter because a direct comparison with the experimental data is possible. In LUMPAC, PLQY value is the ratio between the emitted and absorbed light intensities (see Eq. (3)):

$$PLQY = \frac{A_{rad}\eta_{^5D_0}}{\varphi\eta_{S_0}} \qquad (3)$$

where $\eta_{^5D_0}$ and η_{S_0} are the $^5D_0$ and S_0 level populations, while φ correspond to absorption rate. The $^5D_0$ level population depends on the non-radiative decay rate A_{nrad}, which can be obtained from A_{rad} and the experimental lifetime (τ) as $A_{rad} + A_{nrad} = \tau^{-1}$. The radiative decay rate (A_{rad}) directly depends on the Judd-Ofelt intensity parameters. Thus, the theoretical PLQY is related to the experimental lifetime ad emission spectrum.

The inspection of data reported in Table 1 reveals the substantial difference between A_{rad} and A_{nrad} values for both complexes. Moreover, the **EuL$_3$E$_2$** A_{nrad} value (15814 s^{-1}) is larger than the A_{rad} one (661 s^{-1}), while the opposite is true for **EuL$_3$T$_2$** (4712 s^{-1} and 1143 s^{-1} for A_{nrad} and A_{rad}, respectively). Such a difference can be explained by referring, in the former complex, to the presence of the O–H oscillators, which accounts for the lower PLQY and quantum efficiency. Theoretical outcomes herein reported allow us to gain further details on the radiative and non-radiative process: the **EuL$_3$E$_2$** A_{rad} value is ~½ the **EuL$_3$T$_2$** one, while the **EuL$_3$E$_2$** A_{nrad} is ~3 the **EuL$_3$T$_2$** one. This result suggests that ancillary ligands such as EtOH or TPPO influence differently radiative and non-radiative processes: they slightly affect the former, while they may significantly affect the latter. Further information about A_{rad} may be gained by referring to the contribution percentage of each Eu^{3+} $^5D_0 \rightarrow {}^7F_J$ transition; in fact, not all transitions equally contribute to the radiative process. In this regard, it can be useful to mention that A_{rad} and A_{nrad} have been calculated in the past for similar Eu^{3+} complexes containing TPPO by using LUMPAC and literature results show similar trends [45, 46]. In the **EuL$_3$E$_2$** (**EuL$_3$T$_2$**) percentages to the radiative decay rate are $^5D_0 \rightarrow {}^7F_1$ = 7.45 (4.31), $^5D_0 \rightarrow {}^7F_2$ = 73.13 (88.52), $^5D_0 \rightarrow {}^7F_3$ = 0.00 (0.00), $^5D_0 \rightarrow {}^7F_4$ = 19.39 (7.14), $^5D_0 \rightarrow {}^7F_5$ = 0.00 (0.00), and $^5D_0 \rightarrow {}^7F_6$ = 0.03 (0.03). These values show that, in both complexes, the $^5D_0 \rightarrow {}^7F_2$ transition has the largest percentage thus providing the major contribution to the radiative process, even if with sizable different percentages. Finally, the populations of the S_0, $^5D_0$ and T_1 states have been calculated for both complexes: $\eta_{S_0}, \eta_{^5D_0}, \eta_{T_1}$ are 0.844, 0.086 and 0.069, respectively, for **EuL$_3$E$_2$** and 0.721, 0.220 and 0.059, respectively, for **EuL$_3$T$_2$**. It is interesting to highlight that the population on S_0 and T_1 levels are quite similar for the two complexes, while the largest variation is on the $^5D_0$ level. This large variation in the population of the emitter level difference justifies the larger calculated quantum yield PLQY value for **EuL$_3$T$_2$** (3.48%) with respect to **EuL$_3$E$_2$** (0.67 %). These values are very close to the experimental ones equal to 5.0% and 0.4%, for **EuL$_3$T$_2$** and **EuL$_3$E$_2$**, respectively.

As far as W_{ET} and W_{BT} are concerned, they have been calculated within the Malta's model [17, 47] by using LUMPAC code (see Table 2). In more detail, W_{ET} and W_{BT} are obtained for the most relevant processes involving the ligand and the Eu^{3+} sides, $S_1 \leftrightarrow {}^5D_4$, $T_1 \leftrightarrow {}^5D_1$ and $T_1 \leftrightarrow {}^5D_0$ and they are presented in Table 2 and in Figs. S14 and S15.

The position of the excited states involved in the ET mechanism makes W_{ET} and W_{BT} very similar in both **EuL$_3$E$_2$** and **EuL$_3$T$_2$**. The first possible path to populate the $^5D_0$ state is the ET from S_1 to $^5D_4$. The $S_1 \rightarrow {}^5D_4$ W_{ET} is 10^4

Table 2: Energy transfer (W_{ET}) and back energy transfer (W_{BT}) rates calculated within the Malta's model by using LUMPAC code for **EuL$_3$E$_2$** and **EuL$_3$T$_2$**. S_1 and T_1 energies have been evaluated at the TD-DFT SAOP and AT levels of theory, respectively.

Ligand state (cm^{-1})	Eu^{3+} *4f* state (cm^{-1})	EuL$_3$E$_2$		EuL$_3$T$_2$	
		W_{ET} rate (s^{-1})	W_{BT} rate (s^{-1})	W_{ET} rate (s^{-1})	W_{BT} rate (s^{-1})
S_1 (25,986)	$^5D_4$ (27,583)	3.08×10^4	6.64×10^7	3.96×10^4	8.54×10^7
T_1 (17,922)	$^5D_1$ (18,973)	9.05×10^3	1.82×10^6	1.12×10^4	2.24×10^6
T_1 (17,922)	$^5D_0$ (17,227)	1.84×10^4	9.00×10^2	2.27×10^4	1.11×10^3

s^{-1}, definitely slower than the $S_1 \rightarrow T_1$ inter-system crossing (rate = 10^8 s^{-1}) [48], which cancels the former path weight. Such a peculiar behaviour is determined by the relative position of the $^5D_4$ state, higher in energy than the S_1 one by ~2000 cm^{-1}. The T_1 state is populated at the expense of the $^5D_4$ one and the main ET paths are from **L** T_1 to Eu^{3+} lower excited states ($^5D_1$ and $^5D_0$). A second possible alternative path to populate the $^5D_0$ state is the ET from T_1 to $^5D_1$. For both complexes, the $T_1 \rightarrow {}^5D_1$ W_{ET} is 10^4 s^{-1}, while W_{BT} amounts to 10^6 s^{-1}. The latter value is of the same order of magnitude as the $^5D_1 \rightarrow {}^5D_0$ non-radiative rate; thus, back-ET and the non-radiative decay are competitive processes and the $^5D_1$ state may contribute to populating the $^5D_0$ one. The third and final path corresponds to the direct $T_1 \rightarrow {}^5D_0$ ET. For both complexes, the corresponding $W_{ET} = 10^4$ s^{-1}, while $W_{BT} = 10^3$ s^{-1}. The direct ET seems thus to be the process most contributing to the $^5D_0$ state population. Before going on, it can be of some interest to point out that the $T_1 \rightarrow {}^5D_0$ W_{ET} is only twice the $T_1 \rightarrow {}^5D_1$ one. This is due to the peculiar T_1 relative position, whose energy is almost in between the $^5D_0$ and $^5D_1$ ones (see Figs. S14 and S15). Based on the theoretical luminescence parameters, we propose the following **EuL$_3$E$_2$** and **EuL$_3$T$_2$** ET diagram (Fig. 5). Dashed and full lines are associated with nonradiative and radiative paths, respectively, while curve dashed lines account for **L** → Eu^{3+} ET or Eu^{3+}→ **L** back-ET.

In general, an efficient ligand → metal ET implies in Eu^{3+} complexes implies 2500 cm^{-1} < $\Delta E(T_1 - {}^5D_0)$ <4000 cm^{-1} [29]. Thus, in the presence of β-diketonate ligands, the ET is dominated by the exchange Dexter mechanism and W_{ET} is in the order of 10^8 s^{-1} [41, 49]. Moreover, in several diketonate complexes, $E(T_1) > E(^5D_0)$ and $E(T_1) > E(^5D_1)$ so that the $T_1 \rightarrow {}^5D_1$ ET rate becomes the largest one [41]. Conversely, the T_1 state has in the present case a peculiar position relative to the Eu^{3+} $^5D_0$ and $^5D_1$ low-lying excited states. Indeed, $E(T_1) > E(^5D_0)$ by only ~1800 cm^{-1} but $E(T_1) < E(^5D_1)$ by ~1100 cm^{-1}. This evidence implies: (i) $T_1 \rightarrow {}^5D_0$ and $T_1 \rightarrow {}^5D_1$ W_{ET} are rather low (~10^4 s^{-1}) and (ii) the $T_1 \rightarrow {}^5D_1$ W_{ET} is not the largest. Even though a further consequence of the peculiar T_1 relative energy is the low quantum yields, it has to be underlined that **EuL$_3$E$_2$** and **EuL$_3$T$_2$** are extremely sensitive to temperature variations and thus making them useful for technological applications such as molecular thermometers.
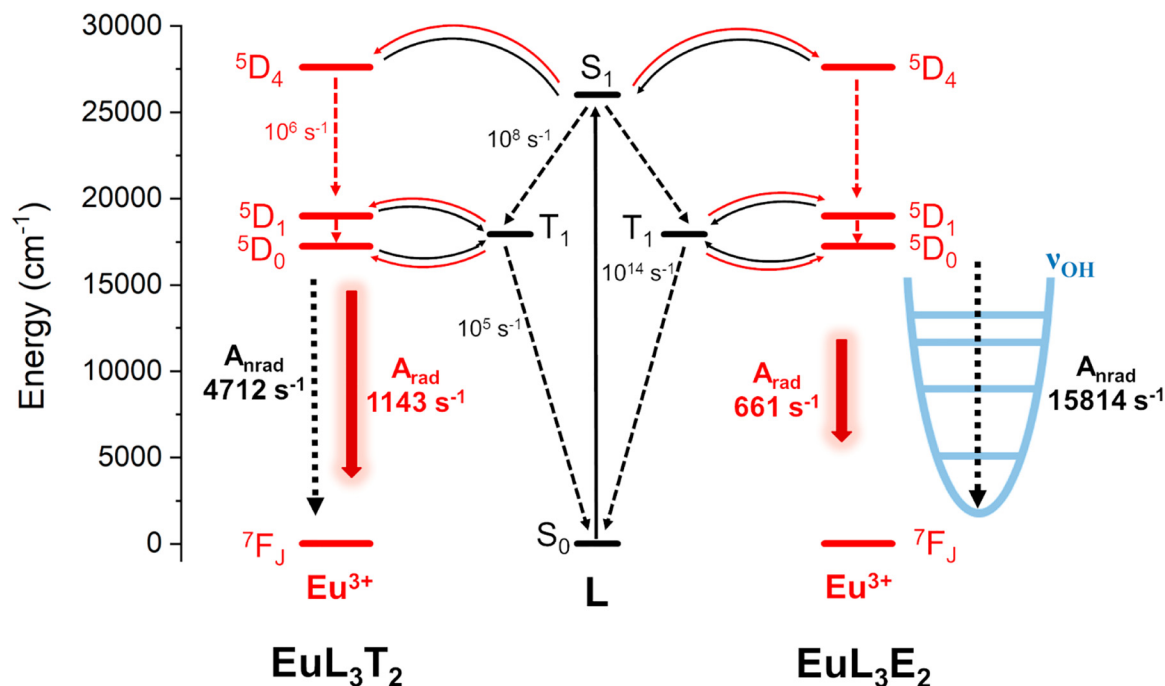

Fig. 5: **EuL$_3$T$_2$** and **EuL$_3$E$_2$** Jablonski energy-level diagram with most relevant ET channels. Theoretical photophysical properties (see also Tables 1 and 2) have been obtained by exploiting the LUMPAC code. Red and black arrows account for **L** → Eu^{3+} ET and Eu^{3+}→ **L** back-ET, respectively. W_{ET} and W_{BT} values are reported in Table 2.
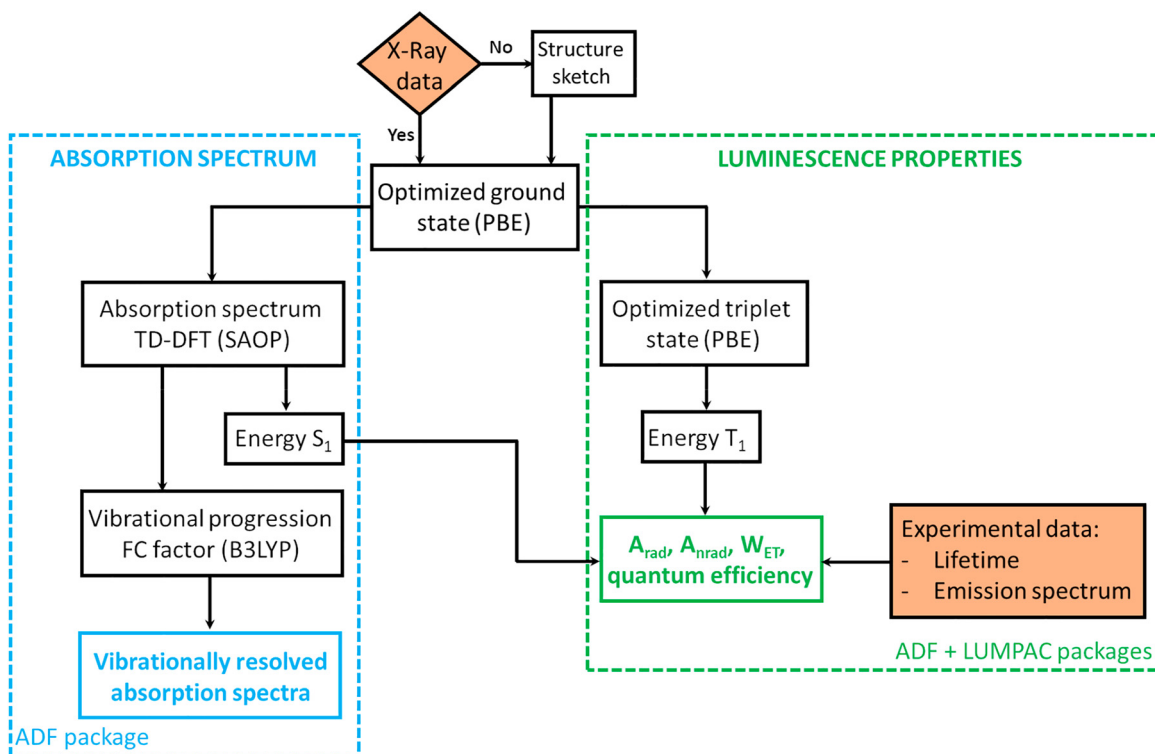
Fig. 6: Flowchart of the computational procedure (with relative functional and packages) for the vibrationally resolved absorption spectrum (blue side) and luminescence properties (green side) for **L** or Eu complexes. The orange boxes are the experimental data.

3 Conclusions

The aim of this study is to present a general theoretical protocol based on DFT calculations to rationalize and possibly drive the design of luminescent Ln^{3+} complexes. Two Eu^{3+} tris(β-diketonate) complexes (**EuL$_3$E$_2$** and **EuL$_3$T$_2$**) with a significantly different luminescence behaviour have been chosen to validate the protocol. **EuL$_3$E$_2$**, besides the tris(β-diketonate) as the main ligand, has two ethanol molecules as ancillary ligands, which are both substituted by triphenylphosphine oxide in **EuL$_3$T$_2$**. The well-known quenching capability of the –OH group, determines a luminescence quantum yield much lower in **EuL$_3$E$_2$** than in **EuL$_3$T$_2$**. The protocol, having as starting points the optimized geometries, the theoretical excited state energies and the experimental lifetimes, is able to quantitatively reproduce quantum yields and calculate A_{rad}, A_{nrad} W_{ET} and W_{BT} (see Fig. 6). Diverse theoretical methodologies and computer packages are combined to insure, at each protocol step, the best agreement between experiment and theory.

Numerical experiments carried out on **L**, **EuL$_3$E$_2$** and **EuL$_3$T$_2$** implied the optimization of their geometries and the modelling of their absorption spectra. Theoretical results have been then compared with corresponding experimental evidence as well as with data pertaining to the analogous Gd^{3+} complexes to obtain the T_1 state. Specifically, absorption spectra and the T_1 energies have been estimated via DFT-based methods, while the emission properties have been modelled by means of the LUMPAC software. Absorption spectra have been mimicked by adopting the PBE geometry and the agreement with structural and spectroscopic data has been found very good. As such, a satisfactory modelling of the **L** absorption spectrum shape needs that vibronic contribution to be taken into account. Two distinct TD-DFT approaches (VT and AT) have been adopted to estimate the T_1 energies. Corresponding calculations have been carried out on **L** as well as on Eu^{3+} and La^{3+} complexes to better take into account minor geometrical variations. The outcomes of these numerical experiments show that the best-suited approach is the AT one. AT **L** triplet energies have been then used to investigate the **EuL$_3$E$_2$** and

EuL₃T₂ IET process. Finally, luminescence properties such as quantum yields, A_{rad}, A_{nrad} energy transfer and back-energy transfer rates contributions have been gained by using the LUMPAC code. Despite this software allowing the optimisation of geometrical parameters and the evaluation of the S_1 and T_1 energies, the T_1 is systematically underestimated thus preventing an efficient energy transfer and good quantum yields. The Hobson choice to have a protocol able to provide quantitative modelling of the energy transfer mechanism in the two complexes has been the use of the TD-DFT, within the AT approach, combined with the LUMPAC code.

In this study, a protocol to investigate the optical properties of Eu^{3+} complexes by starting from the ligand is presented. By the way, the protocol is able to assess whether or not it is sufficient to concentrate on the ligand contributions. These outcomes can be straightforwardly extended to all Eu^{3+} complexes, where the T_1 energy is usually unaffected upon moving from the free **L** to the complex. The estimate of the luminescence behaviour is limited to the evaluation of (i) the optimized geometries, (ii) the absorption spectrum and the energy of the T_1 state, and (iii) the luminescence parameters. The application of the proposed protocol allows the relatively easy determination and screening of luminescence energy transfer processes of different complexes. This additional information could be fruitful to reduce the synthetic efforts to obtain luminescent systems with well-tailored and tuneable properties.

References

[1] W. Levason. *Coord. Chem. Rev.* **340**, 298 (2017). https://doi.org/10.1016/j.ccr.2017.04.003.

[2] P.P. Ferreira da Rosa, Y. Kitagawa, Y. Hasegawa. *Chem. Rev.* **406**, 213153 (2020). https://doi.org/10.1016/j.ccr.2019.213153.

[3] L. Armelao, S. Quici, F. Barigelletti, G. Accorsi, G. Bottaro, M. Cavazzini, E. Tondello. *Coord. Chem. Rev.* **254**, 487 (2010). https://doi.org/10.1016/j.ccr.2009.07.025.

[4] J.C.G. Bünzli, C. Piguet. *Chem. Soc. Rev.* **34**, 1048 (2005). https://doi.org/10.1039/b406082m.

[5] J. Liu, J.S. Miao, H. Bin Wu. *Luminescence* **30**, 393 (2015). https://doi.org/10.1002/bio.2745.

[6] R. Devi, K. Singh, S. Vaidyanathan. *J. Mater. Chem. C* **8**, 8643 (2020). https://doi.org/10.1039/d0tc01360a.

[7] K. Singh, R. Boddula, S. Vaidyanathan. *Inorg. Chem.* **56**, 9376 (2017). https://doi.org/10.1021/acs.inorgchem.7b01565.

[8] J. Vallejo, J. Cano, I. Castro, M. Julve, F. Lloret, O. Fabelo, L. Cañadillas-Delgado, E. Pardo. *Chem. Commun.* **48**, 7726 (2012). https://doi.org/10.1039/c2cc33674j.

[9] F. Cao, Z. Yuan, J. Liu. *J. Ling RSC Adv.* **5**, 102535 (2015). https://doi.org/10.1039/c5ra19710d.

[10] L. Li, Y. Zhu, X. Zhou, C.D.S. Brites, D. Ananias, Z. Lin, F.A.A. Paz, J. Rocha, W. Huang, L.D. Carlos. *Adv. Funct. Mater.* **26**, 8677 (2016). https://doi.org/10.1002/adfm.201603179.

[11] L. Jia, T. Zhou, J. Xu, Z. Xu, M. Zhang, Y. Wang, Z. Li, T. Zhu. *J. Mater. Sci.* **51**, 1324 (2016). https://doi.org/10.1007/s10853-015-9450-x.

[12] V. Fernández-Moreira, B. Song, V. Sivagnanam, A.S. Chauvin, C.D.B. Vandevyver, M. Gijs, I. Hemmilä, H.A. Lehr, J.C.G. Bünzli. *Analyst* **135**, 42 (2009), https://doi.org/10.1039/B922124G.

[13] S. Quici, A. Casoni, F. Foschi, L. Armelao, G. Bottaro, R. Seraglia, C. Bolzati, N. Salvarese, D. Carpanese, A. Rosato. *J. Med. Chem.* **58**, 2003 (2015). https://doi.org/10.1021/jm501945w.

[14] J.C.G. Bünzli, S. V. Eliseeva. *Chem. Sci.* **4**, 1939 (2013). https://doi.org/10.1039/c3sc22126a.

[15] K.Y. Zhang, Q. Yu, H. Wei, S. Liu, Q. Zhao, W. Huang. *Chem. Rev.* **118**, 1770 (2018). https://doi.org/10.1021/acs.chemrev.7b00425.

[16] M.C. Heffern, L.M. Matosziuk, T.J. Meade. *Chem. Rev.* **114**, 4496 (2014). https://doi.org/10.1021/cr400477t.

[17] G.F. de Sá, O.L. Malta, C. de Mello Donegá, A.M. Simas, R.L. Longo, P.A. Santa-Cruz, E.F. da Silva. *Chem. Rev.* **196**, 165 (2000). https://doi.org/10.1016/s0010-8545(99)00054-5.

[18] L. Zhou, Y. Jiang, R. Cui, Y. Li, X. Zhao, R. Deng, H. Zhang. *J. Lumin.* **170**, 692 (2016). https://doi.org/10.1016/j.jlumin.2015.02.053.

[19] A. Carlotto, L. Babetto, S. Carlotto, M. Miozzi, R. Seraglia, M. Casarin, G. Bottaro, M. Rancan, L. Armelao. *ChemPhotoChem* **4**, 674 (2020), https://doi.org/10.1002/cptc.202000116.

[20] P.K. Shahi, A.K. Singh, S.B. Rai, B. Ullrich. *Sens. Actuators A Phys.* **222**, 255 (2015). https://doi.org/10.1016/j.sna.2014.12.021.

[21] J. Sun, B. Song, Z. Ye, J. Yuan. *Inorg. Chem.* **54**, 11660 (2015). https://doi.org/10.1021/acs.inorgchem.5b02458.

[22] J.D.L. Dutra, T.D. Bispo, R.O. Freire. *J. Comput. Chem.* **35**, 772 (2014). https://doi.org/10.1002/jcc.23542.

[23] R.Q. Albuquerque, N.B. da Costa, R.O. Freire. *J. Lumin.* **131**, 2487 (2011). https://doi.org/10.1016/j.jlumin.2011.06.013.

[24] R.O. Freire, F.R.G. Silva, M.O. Rodrigues, M.E. de Mesquita, N.B. da Costa. *J. Mol. Model.* **12**, 16 (2005). https://doi.org/10.1007/s00894-005-0280-7.

[25] M. Hatanaka, A. Osawa, T. Wakabayashi, K. Morokuma, M. Hasegawa. *Chem. Chem. Phys.* **20**, 3328 (2018). https://doi.org/10.1039/c7cp06361j.

[26] L. Babetto, S. Carlotto, A. Carlotto, M. Rancan, G. Bottaro, L. Armelao, M. Casarin. *Dalton Trans.* **49**, 14556 (2020). https://doi.org/10.1039/d0dt02624g.

[27] L. Babetto, S. Carlotto, A. Carlotto, M. Rancan, G. Bottaro, L. Armelao, M. Casarin. *Inorg. Chem.* **60**, 315 (2021). https://doi.org/10.1021/acs.inorgchem.0c02956.

[28] S. Carlotto, L. Babetto, M. Bortolus, A. Carlotto, M. Rancan, G. Bottaro, L. Armelao, D. Carbonera, M. Casarin. *Inorg. Chem.* **60**, 50 (2021). https://doi.org/10.1021/acs.inorgchem.1c01123.

[29] M. Latva, H. Takalob, V.M. Mukkala, C. Matachescu, J.C. Rodríguez-Ubis, J. Kankare. *J. Lumin.* **75**, 149 (1997). https://doi.org/10.1016/s0022-2313(97)00113-0.

[30] C.D.S. Brites, A. Millán, L.D. Carlos. Lanthanides in Luminescent Thermometry, in *Handbook on the Physics and Chemistry of Rare Earths*, **49**, pp. 339–427, Elsevier Science B.V., Amsterdam (2016).

[31] C.D.S. Brites, S. Balabhadra, L.D. Carlos. *Adv. Opt. Mater.* **7**, 1801239 (2019). https://doi.org/10.1002/adom.201801239.

[32] J. Rocha, C.D.S. Brites, L.D. Carlos. *Chem. – Eur. J.* **22**, 14782 (2016). https://doi.org/10.1002/chem.201600860.

[33] C. Bradac, S. Fang Lim, H.-C. Chang, I. Aharonovich, C. Bradac, I. Aharonovich, A.S.F. Lim, H. Chang. *Adv. Opt. Mater.* **8**, 2000183 (2020). https://doi.org/10.1002/adom.202000183.

[34] C.D.S. Brites, P.P. Lima, N.J.O. Silva, A. Millán, V.S. Amaral, F. Palacio, L.D. Carlos. *Nanoscale* **4**, 4799 (2012). https://doi.org/10.1039/c2nr30663h.

[35] L. Armelao, A. Carlotto, F. Mian, J. Tessarolo, G. Bottaro, M. Rancan. *Can. J. Chem.* **95**, 1183 (2017). https://doi.org/10.1139/cjc-2017-0200.

[36] A.S. Amant, W.D. Cornell, P.A. Kollman, T.A. Halgren. *J. Comput. Chem.* **16**, 1483 (1995), https://doi.org/10.1002/jcc.540161206.

[37] J. Frank. in *Introduction to Computational Chemistry*, p. 660, John Wiley & Sons, West Sussex, 3rd ed. (2017).

[38] G. Zhang, C.B. Musgrave. *J. Phys. Chem. A* **111**, 1554 (2007). https://doi.org/10.1021/jp061633o.

[39] M.A. Marques, C.A. Ullrich, F. Nogueira, A. Rubio, K. Burke, E.K. Gross. in *Time-Dependent Density Functional Theory*, 706, Springer, Berlin, Heidelberg (2006).

[40] Y. Suwa, M. Yamaji. *J. Photochem. Photobiol. A Chem.* **316**, 69 (2016). https://doi.org/10.1016/j.jphotochem.2015.10.010.

[41] J.C.A. Júnior, G.L. dos Santos, M. V. Colaço, R.C. Barroso, F.F. Ferreira, M. V. dos Santos, N.R. de Campos, M. V. Marinho, L.T. Jesus, R.O. Freire, L.F. Marques. *J. Phys. Chem. C* **124**, 9996 (2020). https://doi.org/10.1021/acs.jpcc.0c01374.

[42] C. Daiguebonne, A. Deluzet, M. Camara, K. Boubekeur, N. Audebrand, Y. Gérault, C. Baux, O. Guillou. *Cryst. Growth Des.* **3**, 1015 (2003). https://doi.org/10.1021/cg020060b.

[43] D. Jacquemin, E.A. Perpète, I. Ciofini, C. Adamo. *J. Chem. Theory Comput.* **6**, 1532 (2010). https://doi.org/10.1021/ct100005d.

[44] F. Gutierrez, C. Tedeschi, L. Maron, J.P. Daudey, R. Poteau, J. Azema, P. Tisnès, C. Picard. *Dalton Trans.* **1334** (2004), https://doi.org/10.1039/B316246J.

[45] A.I.S. Silva, V.F.C. Santos, N.B.D. Lima, A.M. Simas, S.M.C. Gonçalves. *RSC Adv.* **6**, 90934 (2016). https://doi.org/10.1039/c6ra20609c.

[46] N.B.D. Lima, J.D.L. Dutra, S.M.C. Goncalves, R.O. Freire, A.M. Simas. *Sci. Rep.* **6**, 1 (2016). https://doi.org/10.1038/srep21204.

[47] O.L. Malta. *J. Lumin.* **71**, 229 (1997). https://doi.org/10.1016/s0022-2313(96)00126-3.

[48] J.R. Lakowicz. in *Principles of Fluorescence Spectroscopy*, pp. 1–954, Springer, New York (2006).

[49] I.J. Al-Busaidi, R. Ilmi, J.D.L. Dutra, W.F. Oliveira, A. Haque, N.K. Al Rasbi, F. Marken, P.R. Raithby, M.S. Khan. *Dalton Trans*. **50**, 1465 (2021). https://doi.org/10.1039/d0dt04198j.